Research Article Vol. 9, No. 2 / February 2022 / Optica 145

# Generation and characterization of isolated attosecond pulses at 100 kHz repetition rate

Tobias Witting,[1,*] Mikhail Osolodkov,[1] Felix Schell,[1] Felipe Morales,[1] Serguei Patchkovskii,[1] Peter Šušnjar,[1] Fabio H. M. Cavalcante,[2] Carmen S. Menoni,[2] Claus P. Schulz,[1] Federico J. Furch,[1,3] and Marc J. J. Vrakking[1]

[1]Max Born Institute for Nonlinear Optics and Short Pulse Spectroscopy, Max-Born-Strasse 2A, 12489 Berlin, Germany
[2]Department of Electrical and Computer Engineering, Colorado State University, Fort Collins, Colorado 80523, USA
[3]e-mail: furch@mbi-berlin.de
*Corresponding author: tobias.witting@mbi-berlin.de

Received 15 September 2021; revised 30 November 2021; accepted 19 December 2021; published 28 January 2022

**The generation of coherent light pulses in the extreme ultraviolet (XUV) spectral region with attosecond pulse durations constitutes the foundation of the field of attosecond science. Twenty years after the first demonstration of isolated attosecond pulses, they continue to be a unique tool enabling the observation and control of electron dynamics in atoms, molecules, and solids. It has long been identified that an increase in the repetition rate of attosecond light sources is necessary for many applications in atomic and molecular physics, surface science, and imaging. Although high harmonic generation (HHG) at repetition rates exceeding 100 kHz, showing a continuum in the cutoff region of the XUV spectrum, was already demonstrated in 2013, the number of photons per pulse was insufficient to perform pulse characterization via attosecond streaking, let alone to perform a pump-probe experiment. Here we report on the generation and full characterization of XUV attosecond pulses via HHG driven by near-single-cycle pulses at a repetition rate of 100 kHz. The high number of $10^6$ XUV photons per pulse on target enables attosecond electron streaking experiments through which the XUV pulses are determined to consist of a dominant single attosecond pulse. These results open the door for attosecond pump-probe spectroscopy studies at a repetition rate 1 or 2 orders of magnitude above current implementations.** 

https://doi.org/10.1364/OPTICA.443521

## 1. INTRODUCTION

Extreme ultraviolet (XUV) light pulses generated via high-order harmonic generation (HHG) [1], consisting of attosecond pulse trains (APTs) [2,3] or isolated attosecond pulses (IAPs) [4], have led to the establishment of the field of attosecond science [5]. The HHG process can be described by an intuitive three-step model [6], in which the strong electric field of the laser interacting with a gas of atoms first induces tunnel ionization. The created electron wave packet is accelerated by the electric field of the laser, first away and then back toward its parent ion, and then recombines with the parent ion, releasing the gained kinetic energy in the form of high energy photons at odd multiples of the driving laser frequency. Since the process is repeated every half-cycle of the laser for which the peak intensity is sufficient to ionize the atom, HHG naturally gives rise to a train of attosecond pulses. As the duration of the driving pulse is reduced, the number of pulses in the APT also decreases. If the driving pulse duration approaches a single oscillation of the optical field, and if it is possible to control the carrier-envelope phase (CEP) of the driving pulses, the XUV emission can be confined to a single half-cycle [4,7–9]. IAPs generated in this manner have been successfully implemented to observe light-induced electron tunneling in atoms in real time [10], to follow the valence electron motion in an excited ion [11], and to control electron localization in a dissociating molecule with attosecond precision [12], among many other outstanding examples.

In all the aforementioned examples, and in the majority of experimental setups used for attosecond science, the driving pulses for HHG are produced by a Ti:sapphire chirped pulse amplification (CPA) system followed by non-linear post-compression in a gas-filled hollow-core fiber (HCF) [13], which allows reaching pulse durations near a single optical cycle (2.67 fs at 800 nm) with pulse energies of at least a few μJ. Typical observables in attosecond pump-probe experiments are either the XUV absorption spectrum or the kinetic energy and/or angular distributions of ions or electrons. While these schemes provide valuable information, many research questions call for more sophisticated experimental approaches. In particular, in experiments with atomic and molecular targets in the gas phase, it is highly attractive to implement electron-ion coincidence detection schemes [14], which give access to the fully correlated three-dimensional momentum distributions of all charged particles produced during a photoionization experiment. The technique requires that only one photoionization event is produced per laser pulse in order to avoid the detection of false coincidences, i.e., ions and electrons that are

measured in coincidence but that originate from different parent atoms/molecules. In practice, this requires working at a maximum event rate of approximately 0.2 times the repetition rate of the light source. It follows that high repetition rate light sources are required for these types of experiments to keep data acquisition times manageable. So far, the implementation of coincidence detection in attosecond experiments has been limited to setups working with Ti:sapphire CPAs running at $\leq$10 kHz [15], where the technique has been successfully applied to the study of small molecular systems [16,17]. However, more complex problems involving the study of low probability ionization or dissociation channels require higher repetition rates. Furthermore condensed phase experiments such as photoelectron emission microscopy (PEEM) [18] and attosecond photoelectron streaking [19,20] at surfaces would also benefit from high repetition rate attosecond XUV sources. Since a high number of photoelectrons removed from a surface with a single laser shot has detrimental effects on the energy resolution through space-charge effects, it is advantageous to keep the number of photoelectrons generated per shot low. To achieve high signal-to-noise ratio measurements that go beyond proof of principle experiments, increasing the laser repetition rate is the only viable route.

Ti:sapphire CPAs, delivering CEP-stable, ultrashort pulses with the necessary pulse energies for attosecond pulse generation (typically up to a few mJ) are not scalable beyond 10 kHz. Optical parametric chirped pulse amplifiers (OPCPAs) [21–26] and direct post-compression of high repetition rate ytterbium-based CPAs [27,28] are viable alternatives capable of generating CEP-stable, few-cycle pulses with multi-μJ-level energy, at hundreds of kHz repetition rate. Moreover, OPCPAs have extended the range of CEP-stable, ultrashort pulses with moderate energy and high repetition rate toward the mid-IR region [29–33]. Some high repetition rate OPCPAs operating at 800 nm have been utilized to generate high-order harmonics with a spectrum in the XUV range showing sensitivity to the value of the CEP of the driving pulse [34,35]. Krebs *et al*. [34] demonstrated a continuous XUV spectrum in the cutoff region using 6.6 fs 918 nm pulses from an OPCPA, suggesting the existence of an isolated pulse in this region of the XUV spectrum. However, the number of XUV photons per pulse was not sufficient to carry out pulse characterization with the attosecond streaking technique to determine the temporal structure and pulse duration.

Here we present, to the best of our knowledge, the first demonstration of an attosecond electron streaking experiment driven by XUV pulses operating at 100 kHz repetition rate, i.e., at least an order of magnitude higher than any previous implementation. The ability to do so stems from the available high number of $10^6$ XUV photons per pulse on target, which is comparable to typical attosecond light sources driven by post-compressed Ti:sapphire CPA systems. The temporal structure of the pulse is dominated by a single XUV pulse with sub-140 as duration, demonstrating the suitability of our source for attosecond pump-probe experiments.

## 2. EXPERIMENTAL SETUP

A sketch of the experimental setup is shown in Fig. 1. An OPCPA delivered CEP-stable 7 fs pulses at a central wavelength of 790 nm with up to 190 μJ of energy per pulse and at a repetition rate of 100 kHz [25,36,37]. In HHG, the 7 fs pulses from the OPCPA system, containing 2.6 optical cycles, lead to the generation of short APTs containing seven pulses with varying intensity [38]. To enable efficient amplitude gating of IAPs, the 7 fs OPCPA pulses were compressed to near-single cycle pulse durations, using hollow fiber pulse compression in a 1 m long 340 μm diameter HCF filled with neon gas. The HCF was operated in differential pumping configuration [39–41], i.e., the entrance side was kept at a $\approx 1 \times 10^{-1}$ mbar vacuum, while the exit volume was filled with neon gas at a pressure of 2.5 bar. Dispersion compensation was achieved using chirped mirrors (Ultrafast Innovations, PC70) with a negative group delay dispersion in the range of 500–1050 nm. A pair of ultra-thin fused silica wedges was employed for fine tuning of the dispersion to achieve optimal compression inside the HHG target. The pulse energy after losses in the chirped mirror compressor and the ultra-thin wedges was 95 μJ. Spectra spanning more than one octave supporting 3 fs pulses were achieved. Figure 2 summarizes the spatiotemporal characterization performed with the SEA-F-SPIDER technique [40], which measures the spatially dependent field in one spatial plane, i.e., either $E(x, y_0, t)$ or $E(x_0, y, t)$. As the non-collinear angle of the OPCPA system lies in the horizontal $x$ plane, eventual spatiotemporal couplings would be expected in this plane [36]. In Fig. 2(a), the spatio-spectral intensity distribution $|E(\omega, x, y_0)|^2$ is shown. Apart from small spatial variations (e.g., a frequency-dependent spot size), no significant space-time couplings were observed. In Fig. 2(b), the spatially integrated spectral intensity (red line) and spectral phase

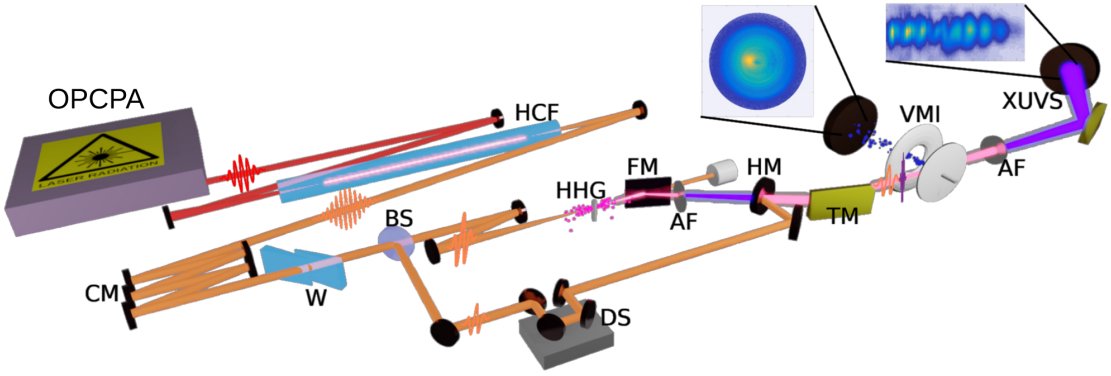


**Fig. 1.** Schematic view of the experimental setup. Pulses from an OPCPA laser system are compressed in a hollow-core fiber (HCF). The pulses are split by a beam splitter (BS). HHG takes place in one arm of the interferometer. The pulses are recombined with a variable delay and focused into the velocity map imaging spectrometer (VMI). CM, chirped mirrors; W, fused silica wedges; DS, delay stage; FM, filter mirror; AF, aluminum filter; HM, holey mirror; TM, toroidal mirror; XUVS, XUV spectrometer.

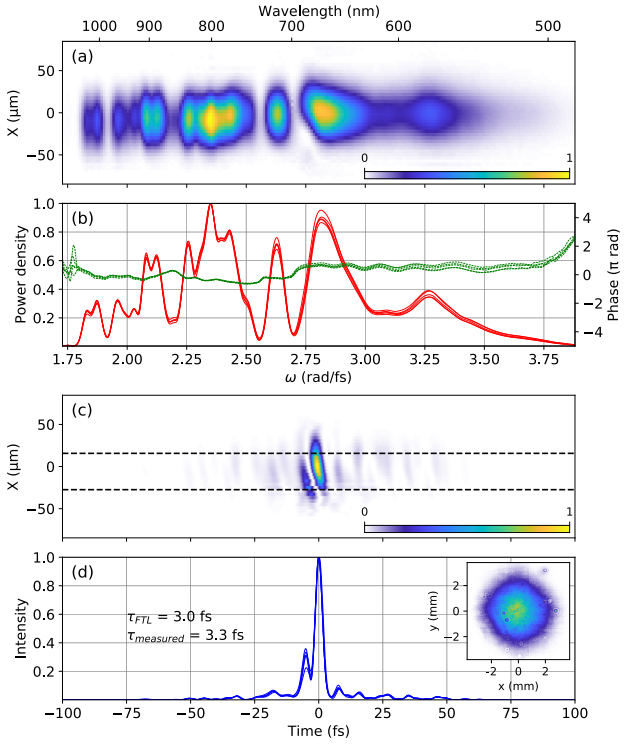


**Fig. 2.** Spatiotemporal characterization of the near-single cycle pulses. (a) Spatio-spectral intensity distribution $|E(x, y_0, \omega)|^2$. (b) Spatially integrated spectral intensity (red line) and spatially integrated spectral phase (green line). Results from five consecutive measurements are shown. (c) Spatiotemporal intensity distribution $|E(x, y_0, t)|^2$. (d) Spatially integrated temporal intensity profile (blue line); results from five consecutive measurements are plotted. The inset in (d) shows the spatial near-field beam profile on a CMOS camera.

(green line) are shown for a series of five measurements acquired over the space of 1 min, demonstrating the excellent short-term stability of the source. The central wavelength is 760 nm. The spectral phase is flat within the compression range of the chirped mirrors form 500 to 1050 nm and shows small oscillations caused by the chirped mirror compressor. Figure 2(c) shows the spatiotemporal intensity profile, and Fig. 2(d) shows the spatially integrated temporal intensity. The pulse duration is $3.3 \pm 0.1$ fs, corresponding to only 1.3 optical cycles. The inset of Fig. 2(d) shows the near-field spatial profile of the beam after the HCF and chirped mirror compressor measured by a CMOS camera.

The near-single-cycle near-infrared (NIR) pulses were sent to an attosecond beamline sketched in Fig. 1 and described in detail in [38]. The pulses were split with the majority of the pulse energy used for HHG. For this, the near-single-cycle pulses were focused to an approximate intensity of $2 \times 10^{14}$ W/cm$^2$ inside a cylindrical gas cell with a diameter of 2 mm, filled with krypton at a backing pressure of 70 mbar. The optimum CEP was chosen by fine tuning the compression (see Supplement 1).

After HHG, the XUV and remaining NIR radiation were separated utilizing a specially designed multilayer dielectric coating, consisting of a $Ta_2O_5/SiO_2$ stack topped by a 200 nm thick layer of $SiO_2$, which acts as a broadband antireflection (AR) coating for the NIR part of the spectrum. At the grazing incidence angle of 75°, the top layer of the coating acts like a bulk mirror for the XUV and has an average reflectivity of 45% in the 20–60 eV spectral range. After the filtering mirror, an Al filter blocks the remaining NIR radiation.

The smaller portion of the NIR energy was used as probe beam. A piezo translation stage in the probe arm was used to provide a variable delay. XUV and NIR pulses were recombined with a holey mirror. Both beams were focused into the experimental chamber by a gold-coated toroidal mirror. The spectrally integrated photon flux on target for the experiment was measured with an XUV photodiode and amounted to $10^6$ photons per shot (comparable to typical Ti:sapphire laser driven attosecond setups), which amounted to an unprecedented flux of $10^{11}$ photons per second on target. In the experimental chamber, the attosecond XUV pulse ionized neon atoms in the presence of a strong NIR probe pulse ($I \approx 4.6$ TW/cm$^2$) and the resulting photoelectron momentum distributions were measured with a velocity map imaging spectrometer (VMI) [42].

## 3. RESULTS

For the characterization of the attosecond XUV pulses, the attosecond streaking technique [43] was employed. Single photon ionization by the XUV pulses launches a photoelectron wave packet into the continuum. In the absence of the NIR pulse, the photoelectron wave packet reproduces the amplitude and phase of the XUV pulses, re-shaped by the photoionization cross section, and shifted in energy by the ionization potential of the target atom. The low photon energy limit of the XUV spectrum, given by the transmission window of the aluminum filter at approximately 15.5 eV, lies a few eV below the ionization threshold of neon (21.56 eV). Therefore, information about the low energy end of the XUV pulse spectrum is lost during photoionization, and the XUV pulse that can be retrieved corresponds to the portion of the spectrum above the ionization potential of neon. The presence of the NIR pulse modulates the photoelectron kinetic energy distribution depending on the value of the NIR field vector potential at the moment of ionization giving rise to a streaking effect. Measurements of the photoelectron kinetic energy distribution at a particular observation angle as a function of XUV-NIR delay (i.e., the electron streaking trace) contain amplitude and phase information on both the NIR and the XUV fields. Within the strong field approximation (SFA), the probability amplitude for producing photoelectrons in the continuum with final momentum $\vec{p}$ is given by [43–45]

$$a(\vec{p}, \tau) = -i \int_{-\infty}^{\infty} \mathrm{d}t \mathrm{d}_{\vec{p}+\vec{A}(t)} E_{\mathrm{XUV}}(t-\tau) \times e^{i[(W+\mathrm{IP})t - \int_t^{\infty} \mathrm{d}t'(\vec{p}\cdot\vec{A}(t') + A(t')^2/2)]}, \quad (1)$$

where $\tau$ is the time-delay between the NIR and XUV fields, $E_{\mathrm{XUV}}$ is the complex amplitude of the electric field of the XUV pulse, $\vec{A}(t)$ is the vector potential of the NIR field, $d_{\vec{p}+\vec{A}(t)}$ is the complex dipole transition matrix element from the ground state to the continuum, IP is the ionization potential of the ionized atom, $\vec{p} + \vec{A}(t)$ is the instantaneous kinetic momentum, and $W = p^2/2$ is the measured photoelectron kinetic energy. Atomic units are used. The measured electron yield in a streaking trace is proportional to $|a(\vec{p}, \tau)|^2$.

Streaking traces for a range of angles with respect to the polarization vector were constructed from the measured photoelectron momentum distributions. For each delay between the XUV and

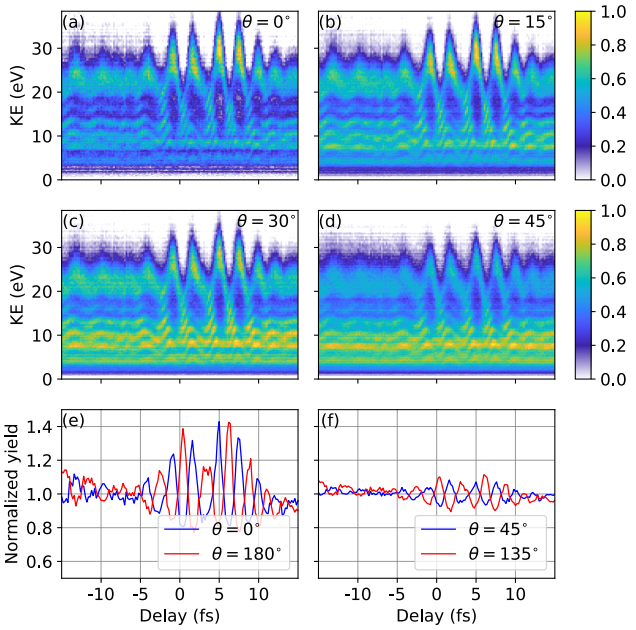


**Fig. 3.** Attosecond electron streaking traces from photoelectron kinetic energy distributions at different observation angles $\theta$ with respect to the laser polarization. (a) $\theta = 0°$, (b) $\theta = 15°$, (c) $\theta = 30°$, and (d) $\theta = 45°$. In all cases, the color scale indicates the electron yield, and it is normalized to the maximum of the trace. (e) and (f) show normalized electron yields as a function of delay for observation angles of 0° and 45°, respectively, and computed in the top and bottom parts of the detector.

NIR pulses, a VMI image was acquired with an integration time of approximately 15 s. Three-dimensional momentum distributions were retrieved from the experimental images by applying an Abel inversion [46] based on the rBASEX algorithm [47,48]. This results in angular distributions described by an expansion of Legendre polynomials. Legendre terms up to order 14 were used to account for the maximum number of photons involved in the strong NIR field dressed photoionization process. The Legendre expansion allows us to build streaking traces at any particular angle with respect to the polarization axis. Streaking traces at angles of 0, 15, 30, 45, 135, 150, 165, and 180° with respect to the laser polarization axis were constructed. A separate experimental image of photoionization of neon by harmonics produced with narrowband XUV pulses obtained by evacuating the hollow fiber was used to calibrate the kinetic energy axis of the VMI spectrometer. Figures 3(a)–3(d) show the photoelectron kinetic energy distributions as a function of XUV-NIR delay, taken at observation angles of 0°, 15°, 30°, and 45°, respectively. The electron streaking traces clearly show the modulation of the photoelectron kinetic energy distributions as a result of the presence of the NIR field during ionization. The spectral modulations with an energy spacing of approximately twice the NIR photon energy $\omega_{\mathrm{NIR}}$ at photon energies below ≈20 eV indicates the presence of satellite pulses at a delay of $\pm T_{\mathrm{NIR}}/2$ from the main XUV pulse. At the same time, the smooth spectrum above ≈20 eV kinetic energy suggests that a clean isolated attosecond pulse exists in this portion of the XUV spectrum.

In order to retrieve the XUV and NIR pulses from the experimental trace, most retrieval methods replace the product $\vec{p} \cdot \vec{A}(t)$ in Eq. (1) by $\vec{p}_o \cdot \vec{A}(t)$, with $\vec{p}_o$, the central momentum of the kinetic energy distribution. This central momentum approximation (CMA) leads to an overestimation of the strength of the streaking effect at low kinetic energies. Validity of the CMA requires the central momentum of the kinetic energy distribution to be considerably larger than its bandwidth ($|\vec{p}_o| >> \Delta p$), a condition that is certainly not met in the measurements shown in Fig. 3. Therefore, the Volkov-transform generalized projection algorithm (VTGPA) [49] was chosen as the retrieval method to analyze the experimental data. The VTGPA method determines an explicit solution for $E_{\mathrm{XUV}}(t)$ by finding a local minimum of an error function (or a figure of merit expression) [49]. If the error function for a particular streaking trace contains many local minima, the solution of the VTGPA may converge to any of those minima. Therefore, to complement the analysis of our data sets by the VTGPA, an alternative method was developed, based on a global optimization routine. This method, which we call streaking global optimization (SGO) guesses the XUV spectrum from a weakly streaked region of the experimental trace and utilizes equation Eq. (1) and standard global optimization routines to fit the spectral phase. The attosecond pulse retrieval algorithms and the data processing are discussed in detail in Supplement 1.

Note that equation Eq. (1) assumes that the effect of the attractive Coulomb field on the escaping photoelectron can be neglected and, furthermore, that the only ionization pathway is single photon ionization by the XUV field. As a result of the second assumption and due to the phase term $\vec{p} \cdot \vec{A}(t)$, it is expected that electron streaking traces at different observation angles differ in the strength of the streaking effect, as observed in the traces shown in Figs. 3(a)–3(d). Additional differences in the shape of the photoelectron spectra arise due to the angle-dependence of the dipole transition matrix element. In Figs. 3(a)–3(d), the relative spectral amplitude at lower photoelectron energies increases with the angle. In addition, inspection of the energy-integrated electron yield as a function of the XUV-NIR delay shows a strong modulation of the yield in the regions where the streaking field is strongest. This modulation has an opposite sign in the top and bottom portions of the streaking trace. Due to the strong NIR field and very short pulse duration, one can expect a high degree of ground state polarization by the strong NIR field, which in turn strongly changes the photoionization probability.

In order to assess the validity of the VTGPA and the SGO in the presence of the aforementioned effects in the experimental data, the algorithms were first applied to simulated streaking traces, that where obtained by numerically solving the time-dependent Schrödinger equation (TDSE) in the single-active electron approximation, with an effective potential for neon [50]. Analysis of the simulated results shows that both methods are able to satisfactorily retrieve the input XUV field with a relative pulse field error for normalized fields [51] on the order of 0.1. Further details can be found in Supplement 1.

The VTGPA and SGO methods were applied to a set of experimental traces at different observation angles. In total, 32 different experimental traces were analyzed with each retrieval method. More details about the data processing and the analysis are presented in Supplement 1. Figure 4 shows a summary of the results. Figures 4(a) and 4(c) show the absolute value squared of the average XUV pulse envelope retrieved with the VTGPA and the SGO algorithms, respectively. A confidence region of $\pm 1\sigma$ is indicated by the light blue shaded area, which is not visible on a linear scale. The pulse retrievals by the VTGPA result in an average pulse duration of $132 \pm 5$ as FWHM, while the SGO algorithm retrieves XUV pulses with a FWHM of $124 \pm 3$ as. The insets in Figs. 4(a) and

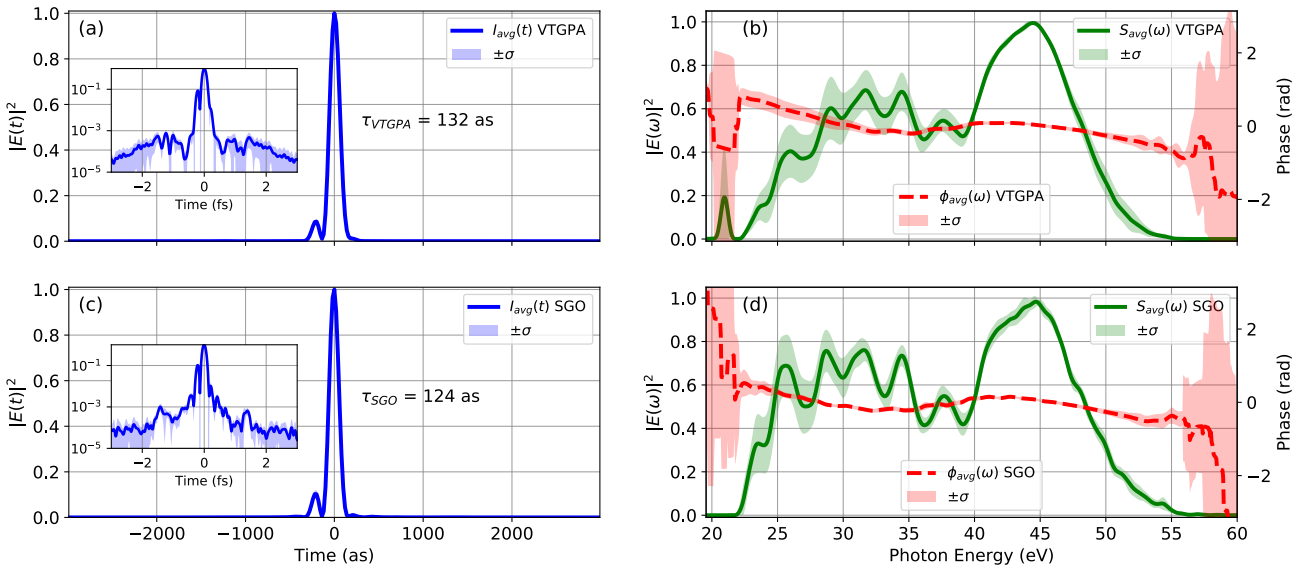


**Fig. 4.** Retrieval of the XUV IAPs. (a) Retrieved XUV pulse intensity envelope normalized to its maximum value. The blue line corresponds to the average over all VTGPA retrievals, and the shaded area corresponds to 1 standard deviation around the mean (not visible on the linear scale). The inset shows the intensity envelope on a logarithmic scale. (b) Retrieved average spectrum (green) and spectral phase (red dashed line) corresponding to the pulse in (a). The shaded areas correspond to 1 standard deviation around the means. (c) and (d) show the corresponding results found with the SGO retrievals.

4(c) show the temporal intensity profiles on a logarithmic scale. The pre-pulse satellite located at $\approx -1.35$ fs (approximately one half of the NIR laser period) has a relative intensity of $0.7 \times 10^{-3}$ and $1.0 \times 10^{-3}$ for the VTGPA and SGO retrievals, respectively. The post-pulse satellite located at $\approx +1.35$ fs has a relative intensity of $4 \times 10^{-4}$ and $6 \times 10^{-4}$ for the VTGPA and SGO retrievals, respectively. The satellite pre- and post-pulses stem from XUV emission from the two weaker neighboring half-cycles of the NIR field and are not unexpected for purely amplitude gated HHG. The satellite pulses are discussed in more detail in Section S5 of Supplement 1. The extremely low relative intensity of the satellite pulses underscores the usefulness of our source for attosecond pump-probe experiments. Figures 4(b) and 4(d) show the retrieval results in the spectral domain. The mean of the retrieved spectral intensities is plotted as a dark green line with the confidence region of $\pm 1\sigma$ indicated by the light green shaded area. Note that the spectrum shown in Fig. 4(b) (SGO retrieval) is an experimental spectrum, whereas the spectrum shown in Fig. 4(d) is the spectrum retrieved by the VTGPA method. Therefore, a comparison between these spectra serves as a sanity check for the output of the VTGPA method. Similarly, the means of the spectral phases are plotted as dark red dashed lines, with the $\pm 1\sigma$ confidence intervals as light red shaded areas. In both cases, the phases are essentially flat with a residual negative third-order component, as is expected for XUV pulses near the cutoff region with phase-matching favoring the short trajectories [52]. Individual reconstructed streaking traces are shown in Supplement 1.

## 4. CONCLUSION

In summary, we have demonstrated the generation and characterization of high flux isolated attosecond XUV pulses at an unprecedented repetition rate of 100 kHz. This was achieved by direct amplitude gating of HHG using near-single-cycle (3.3 fs) driving pulses obtained by hollow fiber compression of pulses from an OPCPA laser system. The high XUV photon flux of our source allowed performing attosecond electron streaking experiments. The measured streaking traces clearly indicate the presence of isolated XUV pulses, which have been retrieved utilizing two different retrieval algorithms, previously tested by analyzing simulated streaking traces generated by numerically solving the TDSE. It is envisioned that this high repetition rate source of attosecond pulses will enable attosecond pump-probe spectroscopy studies with electron-ion coincidence detection, allowing data collection speeds 1 order of magnitude higher than currently operating systems.

**Funding.** U.S. Department of Defense (ONR N00014-17-1-2536); Horizon 2020 Framework Programme (674960).

**Acknowledgment.** The authors thank R. Peslin, A. Loudovici, and Ch. Reiter for technical support.

**Disclosures.** The authors declare no conflicts of interest.

**Data availability.** Data underlying the results presented in this paper are not publicly available at this time but may be obtained from the authors upon reasonable request.

**Supplemental document.** See Supplement 1 for supporting content.

## REFERENCES

1. M. Ferray, A. L'Huillier, X. F. Li, L. A. Lompre, G. Mainfray, and C. Manus, "Multiple-harmonic conversion of 1064 nm radiation in rare gases," J. Phys. B **21**, L31–35 (1988).
2. P. Corkum, N. Burnett, and M. Ivanov, "Subfemtosecond pulses," Opt. Lett. **19**, 1870–1872 (1994).
3. P. Antoine, A. L'Huillier, and M. Lewenstein, "Attosecond pulse trains using high–order harmonics," Phys. Rev. Lett. **77**, 1234–1237 (1996).
4. M. Hentschel, R. Kienberger, C. Spielmann, G. A. Reider, N. Milosevic, T. Brabec, P. Corkum, U. Heinzmann, M. Drescher, and F. Krausz, "Attosecond metrology," Nature **414**, 509–513 (2001).
5. F. Krausz and M. Ivanov, "Attosecond physics," Rev. Mod. Phys. **81**, 163–234 (2009).
6. P. B. Corkum, "Plasma perspective on strong field multiphoton ionization," Phys. Rev. Lett. **71**, 1994–1997 (1993).
7. G. Sansone, E. Benedetti, F. Calegari, C. Vozzi, L. Avaldi, R. Flammini, L. Poletto, P. Villoresi, C. Altucci, R. Velotta, S. Stagira, S. De Silvestri, and

M. Nisoli, "Isolated single-cycle attosecond pulses," Science **314**, 443–446 (2006).
8. K. T. Kim, C. Zhang, T. Ruchon, J.-F. Hergott, T. Auguste, D. M. Villeneuve, P. B. Corkum, and F. Quéré, "Photonic streaking of attosecond pulse trains," Nat. Photonics **7**, 651–656 (2013).
9. T. Pfeifer, A. Jullien, M. J. Abel, P. M. Nagel, L. Gallmann, D. M. Neumark, and S. R. Leone, "Generating coherent broadband continuum soft-X-ray radiation by attosecond ionization gating," Opt. Express **15**, 17120–17128 (2007).
10. M. Uiberacker, T. Uphues, M. Schultze, A. J. Verhoef, V. Yakovlev, M. F. Kling, J. Rauschenberger, N. M. Kabachnik, H. Schröder, M. Lezius, K. L. Kompa, H.-G. Muller, M. J. J. Vrakking, S. Hendel, U. Kleineberg, U. Heinzmann, M. Drescher, and F. Krausz, "Attosecond real-time observation of electron tunnelling in atoms," Nature **446**, 627–632 (2007).
11. E. Goulielmakis, Z.-H. Loh, A. Wirth, R. Santra, N. Rohringer, V. S. Yakovlev, S. Zherebtsov, T. Pfeifer, A. M. Azzer, M. F. Kling, S. R. Leone, and F. Krausz, "Real-time observation of valence electron motion," Nature **466**, 739–743 (2010).
12. G. Sansone, F. Kelkensberg, J. F. Pérez-Torres, F. Morales, M. F. Kling, W. Siu, O. Ghafur, P. Johnsson, M. Swoboda, E. Benedetti, F. Ferrari, F. Lépine, J. L. Sanz-Vicario, S. Zherebtsov, I. Znakovskaya, A. L'Huillier, M. Y. Ivanov, M. Nisoli, F. Martín, and M. J. J. Vrakking, "Electron localization following attosecond molecular photoionization," Nature **465**, 763–766 (2010).
13. M. Nisoli, S. D. Silvestri, O. Svelto, R. Szipöcs, K. Ferencz, C. Spielmann, S. Sartania, and F. Krausz, "Compression of high-energy laser pulses below 5 fs," Opt. Lett. **22**, 522–524 (1997).
14. J. Ullrich, R. Moshammer, A. Dorn, R. Dorner, L. Schmidt, and H. Schmidt-Bocking, "Recoil-ion and electron momentum spectroscopy: reaction-microscopes," Rep. Prog. Phys. **66**, 1463–1545 (2003).
15. M. Sabbar, S. Heuser, R. Boge, M. Lucchini, L. Gallmann, C. Cirelli, and U. Keller, "Combining attosecond XUV pulses with coincidence spectroscopy," Rev. Sci. Instrum. **85**, 103113 (2014).
16. L. Cattaneo, J. Vos, R. Y. Bello, A. Palacios, S. Heuser, L. Pedrelli, M. Lucchini, C. Cirelli, F. Martín, and U. Keller, "Attosecond coupled electron and nuclear dynamics in dissociative ionization of H2," Nat. Phys. **14**, 733–738 (2018).
17. J. Vos, L. Cattaneo, S. Patchkovskii, T. Zimmermann, C. Cirelli, M. Lucchini, A. Kheifets, A. S. Landsman, and U. Keller, "Orientation-dependent stereo Wigner time delay and electron localization in a small molecule," Science **360**, 1326–1330 (2018).
18. M. I. Stockman, M. F. Kling, U. Kleineberg, and F. Krausz, "Attosecond nanoplasmonic-field microscope," Nat. Photonics **1**, 539–544 (2007).
19. A. L. Cavalieri, N. Müller, T. Uphues, V. S. Yakovlev, A. Baltuška, B. Horvath, B. Schmidt, L. Blümel, R. Holzwarth, S. Hendel, M. Drescher, U. Kleineberg, P. M. Echenique, R. Kienberger, F. Krausz, and U. Heinzmann, "Attosecond spectroscopy in condensed matter," Nature **449**, 1029–1032 (2007).
20. W. A. Okell, T. Witting, D. Fabris, C. A. Arrell, J. Hengster, S. Ibrahimkutty, A. Seiler, M. Barthelmess, S. Stankov, D. Y. Lei, Y. Sonnefraud, M. Rahmani, T. Uphues, S. A. Maier, J. P. Marangos, and J. W. G. Tisch, "Temporal broadening of attosecond photoelectron wavepackets from solid surfaces," Optica **2**, 383–387 (2015).
21. F. J. Furch, A. Giree, F. Morales, A. Anderson, Y. Wang, C. P. Schulz, and M. J. J. Vrakking, "Close to transform-limited, few-cycle 12 μJ pulses at 400 kHz for applications in ultrafast spectroscopy," Opt. Express **24**, 19293–19310 (2016).
22. J. Rothhardt, S. Demmler, S. Hädrich, J. Limpert, and A. Tünnermann, "Octave-spanning OPCPA system delivering CEP-stable few-cycle pulses and 22 W of average power at 1 MHz repetition rate," Opt. Express **20**, 10870–10878 (2012).
23. S. Prinz, M. Haefner, C. Y. Teisset, R. Bessing, K. Michel, Y. Lee, X. T. Geng, S. Kim, D. E. Kim, T. Metzger, and M. Schultze, "CEP-stable, sub-6 fs, 300-kHz OPCPA system with more than 15 W of average power," Opt. Express **23**, 1388–1394 (2015).
24. J. Matyschok, T. Lang, T. Binhammer, O. Prochnow, S. Rausch, M. Schultze, A. Harth, P. Rudawski, C. L. Arnold, A. L'Huillier, and U. Morgner, "Temporal and spatial effects inside a compact and CEP stabilized, few-cycle OPCPA system at high repetition rates," Opt. Express **21**, 29656–29665 (2013).
25. F. J. Furch, T. Witting, A. Giree, C. Luan, F. Schell, G. Arisholm, C. P. Schulz, and M. J. Vrakking, "CEP-stable few-cycle pulses with more than 190 μJ of energy at 100 kHz from a noncollinear optical parametric amplifier," Opt. Lett. **42**, 2495–2498 (2017).
26. S. Hrisafov, J. Pupeikis, P.-A. Chevreuil, F. Brunner, C. R. Phillips, L. Gallmann, and U. Keller, "High-power few-cycle near-infrared OPCPA for soft X-ray generation at 100 kHz," Opt. Express **28**, 40145–40154 (2020).
27. L. Lavenu, M. Natile, F. Guichard, X. Délen, M. Hanna, Y. Zaouter, and P. Georges, "High-power two-cycle ultrafast source based on hybrid nonlinear compression," Opt. Express **27**, 1958–1967 (2019).
28. M. Müller, J. Buldt, H. Stark, C. Grebing, C. Grebing, J. Limpert, J. Limpert, and J. Limpert, "Multipass cell for high-power few-cycle compression," Opt. Lett. **46**, 2678–2681 (2021).
29. J. Pupeikis, P.-A. Chevreuil, N. Bigler, L. Gallmann, C. R. Phillips, and U. Keller, "Water window soft X-ray source enabled by a 25 W few-cycle 2.2 μm OPCPA at 100 kHz," Optica **7**, 168–171 (2020).
30. N. Thiré, R. Maksimenka, B. Kiss, C. Ferchaud, G. Gitzinger, T. Pinoteau, H. Jousselin, S. Jarosch, P. Bizouard, V. D. Pietro, E. Cormier, K. Osvay, and N. Forget, "Highly stable, 15 W, few-cycle, 65 mrad CEP-noise mid-IR OPCPA for statistical physics," Opt. Express **26**, 26907–26915 (2018).
31. M. Neuhaus, H. Fuest, M. Seeger, J. Schötz, M. Trubetskov, P. Russbueldt, H. Hoffmann, E. Riedle, Z. Major, V. Pervak, M. F. Kling, and P. Wnuk, "10 W CEP-stable few-cycle source at 2 μm with 100 kHz repetition rate," Opt. Express **26**, 16074–16085 (2018).
32. U. Elu, M. Baudisch, H. Pires, F. Tani, M. H. Frosz, F. Köttig, A. Ermolov, P. S. Russell, and J. Biegert, "High average power and single-cycle pulses from a mid-IR optical parametric chirped pulse amplifier," Optica **4**, 1024–1029 (2017).
33. M. Mero, Z. Heiner, V. Petrov, H. Rottke, F. Branchi, G. M. Thomas, and M. J. J. Vrakking, "43 W, 1.55 μm and 12.5 W, 3.1 μm dual-beam, sub-10 cycle, 100 kHz optical parametric chirped pulse amplifier," Opt. Lett. **43**, 5246–5249 (2018).
34. M. Krebs, S. Hadrich, S. Demmler, J. Rothhardt, A. Zair, L. Chipperfield, J. Limpert, and A. Tunnermann, "Towards isolated attosecond pulses at megahertz repetition rates," Nat. Photonics **7**, 555–559 (2013).
35. A. Harth, C. Guo, Y.-C. Cheng, A. Losquin, M. Miranda, S. Mikaelsson, C. M. Heyl, O. Prochnow, J. Ahrens, U. Morgner, A. L'Huillier, and C. L. Arnold, "Compact 200 kHz HHG source driven by a few-cycle OPCPA," J. Opt. **20**, 014007 (2017).
36. T. Witting, F. J. Furch, and M. J. Vrakking, "Spatio-temporal characterisation of a 100 kHz 24 W sub-3-cycle NOPCPA laser system," J. Opt. **20**, 044003 (2018).
37. D. Hoff, F. J. Furch, T. Witting, K. Rühle, D. Adolph, A. M. Sayler, M. J. J. Vrakking, G. G. Paulus, and C. P. Schulz, "Continuous every-single-shot carrier-envelope phase measurement and control at 100 kHz," Opt. Lett. **43**, 3850–3853 (2018).
38. M. Osolodkov, F. Furch, F. Schell, P. Šušnjar, F. Cavalcante, C. S. Menoni, C. P. Schulz, T. Witting, and M. J. J. Vrakking, "Generation and characterisation of few-pulse attosecond pulse trains at 100 kHz repetition rate," J. Phys. B **53**, 194003 (2020).
39. A. Suda, M. Hatayama, K. Nagasaka, and K. Midorikawa, "Generation of sub-10-fs, 5-mJ-optical pulses using a hollow fiber with a pressure gradient," Appl. Phys. Lett. **86**, 111116 (2005).
40. T. Witting, F. Frank, C. A. Arrell, W. A. Okell, J. P. Marangos, and J. W. G. Tisch, "Characterization of high-intensity sub-4-fs laser pulses using spatially encoded spectral shearing interferometry," Opt. Lett. **36**, 1680–1682 (2011).
41. W. A. Okell, T. Witting, D. Fabris, D. Austin, M. Bocoum, F. Frank, A. Ricci, A. Jullien, D. Walke, J. P. Marangos, R. Lopez-Martens, and J. W. G. Tisch, "Carrier-envelope phase stability of hollow fibers used for high-energy few-cycle pulse generation," Opt. Lett. **38**, 3918–3921 (2013).
42. O. Ghafur, W. Siu, P. Johnsson, M. F. Kling, M. Drescher, and M. J. Vrakking, "A velocity map imaging detector with an integrated gas injection system," Rev. Sci. Instrum. **80**, 033110 (2009).
43. J. Itatani, F. Quéré, G. L. Yudin, M. Y. Ivanov, F. Krausz, and P. B. Corkum, "Attosecond streak camera," Phys. Rev. Lett. **88**, 173903 (2002).
44. M. Lewenstein, P. Balcou, M. Y. Ivanov, A. L'Huillier, and P. B. Corkum, "Theory of high-harmonic generation by low-frequency laser fields," Phys. Rev. A **49**, 2117–2132 (1994).
45. Y. Mairesse and F. Quere, "Frequency-resolved optical gating for complete reconstruction of attosecond bursts," Phys. Rev. A **71**, 011401 (2005).

46. D. D. Hickstein, S. T. Gibson, R. Yurchak, D. D. Das, and M. Ryazanov, "A direct comparison of high-speed methods for the numerical Abel transform," Rev. Sci. Instrum. **90**, 065115 (2019).
47. M. Ryazanov, "Development and implementation of methods for sliced velocity map imaging. Studies of overtone-induced dissociation and isomerization dynamics of hydroxymethyl radical ($CH_2OH$ and $CD_2OH$)," Ph.D. thesis (University of Southern California, 2012).
48. M. Ryazanov and H. Reisler, "Improved sliced velocity map imaging apparatus optimized for H photofragments," J. Chem. Phys. **138**, 144201 (2013).
49. P. D. Keathley, S. Bhardwaj, J. Moses, G. Laurent, and F. X. Kärtner, "Volkov transform generalized projection algorithm for attosecond pulse characterization," New J. Phys. **18**, 073009 (2016).
50. S. Patchkovskii, M. J. J. Vrakking, D. M. Villeneuve, and H. Niikura, "Selection of the magnetic quantum number in resonant ionization of neon using an XUV-IR two-color laser field," J. Phys. B **53**, 134002 (2020).
51. C. Dorrer and I. A. Walmsley, "Accuracy criterion for ultrashort pulse characterization techniques: application to spectral phase interferometry for direct electric field reconstruction," J. Opt. Soc. Am. B **19**, 1019–1029 (2002).
52. K. Varjú, P. Johnsson, J. Mauritsson, A. L'Huillier, and R. López-Martens, "Physics of attosecond pulses produced via high harmonic generation," Am. J. Phys **77**, 389–395 (2009).